Multi-Star Wavefront Control at the Occulting Mask Coronagraph Testbed: Monochromatic Laboratory Demonstration for the Roman Coronagraph Instrument

Dan Sirbu*[1], Ruslan Belikov [1], Eduardo Bendek[2], David Marx[2], A J Eldorado Riggs[2], Camilo Mejia Prada[2], Byoung-Joon Seo [2], Hanying Zhou [2]

[1]NASA Ames Research Center, Moffett Field, Mountain View, CA

[2]Jet Propulsion Laboratory, California Institute of Technology, Pasadena, CA

ABSTRACT

The Astro2020 decadal survey recommended the Habitable Worlds Observatory (HWO), NASA's direct imaging flagship mission, with a goal to achieve a statistically robust mission yield of 25 or more potentially habitable exoplanets. One way to achieve is to increase the instrument effectiveness by introducing additional bright, nearby targets. A majority of Sun-like stars have a stellar companion that can introduce additional noise into the field of view of any high-contrast imaging instrument and enabling exoplanet discovery around binary stars represents a path to increased coronagraphic instrument efficiency by increasing the available science target pool of bright nearby stars. This includes both of the Alpha Centauri A and B stars which would represent the top science target for direct imaging if companion leakage could be suppressed. Multi-Star Wavefront Control (MSWC) is a technique that removes stellar leakage from both stellar components, enabling direct imaging of exoplanets in many binary star systems which can potentially increase coronagraphic instrument effectiveness

We present the latest testbed results obtained with MSWC as part of the technology development effort focusing on demonstrations conducted on the Occulting Mask Coronagraph (OMC) testbed at JPL during the vacuum test window last winter, with an additional vacuum test planned for this fall. The MSWC mask consists of a shaped pupil mask similar to the one used for the Wide-Field of View mode, but also includes a set of superimposed, regularly-spaced dots that serve as a diffraction grating. OMC has a layout similar to the Roman Space Telescope coronagraph instrument and configured with a binary imaging mode with a MSWC mask using same design as the contributed mask for the Roman coronagraph. Our testbed results represent the first demonstrations of this technique using the recently installed full binary source. We present results demonstrating suppression in the Super-Nyquist regime for the 3rd diffraction order reaching 8.7e-9 contrast with the Roman pupil. In addition, we present results obtained with a physical binary source and running MSWC in a binary star regime demonstrating 9.6e-8 contrast for a geometry matching potential Alpha Centauri observations in a 515 nm monochromatic wavelength (similar but bluer than for Band 1) using the 5th diffraction order. Planned demonstrations in the upcoming vacuum window this fall will focus on Band 3d and Band 4 using the full MSWC mode for an Alpha Centauri geometry.

Keywords: Exoplanets, Deformable Mirrors, High-Contrast Imaging, Binary Stars, Wavefront Control, Roman Coronagraph Instrument, Multi-Star Wavefront Control, Super-Nyquist Wavefront Control

1. INTRODUCTION

The Astro2020 decadal survey recommended the Habitable Worlds Observatory (HWO), NASA's direct imaging flagship mission, with a goal to achieve a statistically robust mission yield of 25 or more potentially habitable exoplanets. One way to achieve this is to increase the instrument effectiveness by introducing additional bright, nearby targets which includes the majority of Sun-like (FGK) stars in binary systems.[1,2] For many of these stars, a stellar companion that is sufficiently bright and closely separated relative to the target component can introduce additional noise into the field of view of any high-contrast imaging instrument limiting achievable

* email: dan.sirbu@nasa.gov

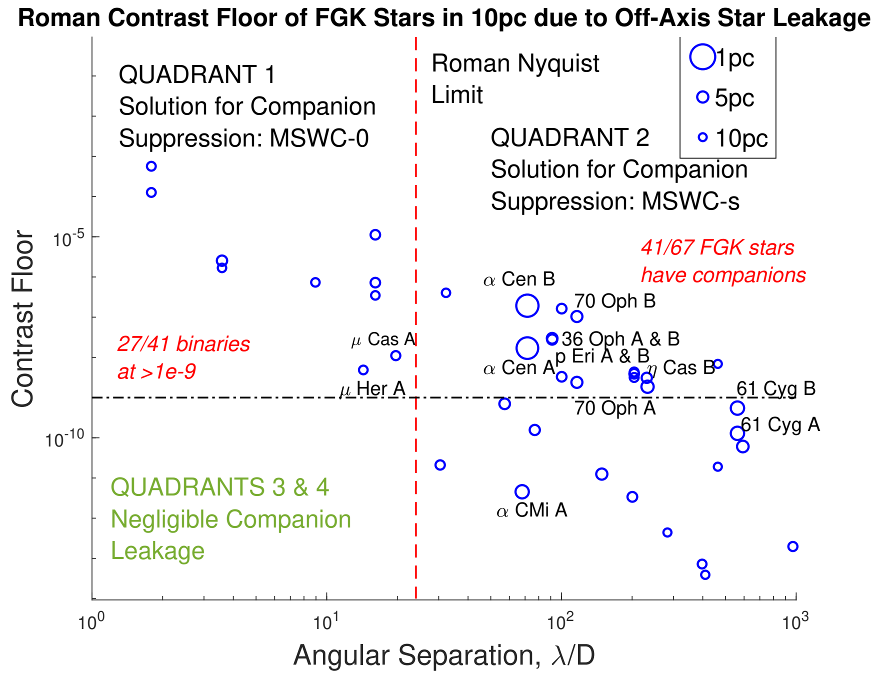

Figure 1: Predicted contrast floor for the Roman coronagraph instrument operating in Band 1 for Sun-like stars with a binary companion located with 10 pc. The horizontal black line indicates an optimistic 1e-9 contrast goal. The vertical red line indicates the Nyquist limit for 48x48 Xinetics DMs.

contrast. These include high-quality target stars such as the A and B components of Alpha Centauri, our nearest stellar neighbor.

Multi-Star Wavefront Control (MSWC) is an algorithmic technique that can be applied to any high-contrast imaging instrument that features an adaptive optics system.[3,4] A set of DM modes removes leakage at sub-Nyquist separations for the target star, while a second non-redundant set of DM modes remove leakage from the off-axis companion. For a widely separated companion outside the nominally controllable spatial limit of the DM (its Nyquist limit), we use a nearby diffraction order from a mild grating. This operating mode outside the spatial Nyquist limit of the DM is called Super-Nyquist Wavefront Control (SNWC).

In addition to enhancing direct imaging yields of HWO by 10-20% (and greater in a target-depleted regime e.g., for an extended mission),[5] MSWC potentially enables the Roman Space Telescope the opportunity to directly image a small, rocky planet if such a planet exists around the Alpha Centauri stars. In Figure 1, we plot the predicted contrast floor for FGK target stars within 10 pc applying the dominant optical aberration PSD profile for the Roman primary in Band 1. 41 target stars have a stellar companion, and 27 out of these are sufficiently bright and nearby to cause a contrast floor greater than 1e-9 (which is slightly better than Roman's current best estimate or CBE level of ∼5-6e-9[6] expected for dimmer nearby stars at Vmag = 5). For the A and B components of Alpha Centauri, suppression by a factor of ∼10 and ∼100 respectively of the companion enables a rocky planet of 1.4 $R_\oplus$ or greater could be observed at a 1e-9 contrast level at gibbous phase.

The minimum detectable radius of an exoplanet at quadrature with the Roman coronagraph instrument around both Alpha Cen A and B across the field of view of the MSWC mask is shown in Figure 2. The top two curves correspond to the minimum detectable radii at Band 1 and Band 4 with the contrast limit given by companion leakage using traditional single-star wavefront control (SSWC). This also shows that even when limited by companion leakage, large planets are detectable with the Roman coronagraph. In particular, around Alpha Centauri A a planet with radius greater than $2R_\oplus$ would be detectable near the inner working angle (IWA) and the NEAR planet candidate[7] with a semimajor axis of 1.1 AU (∼1 year orbital period) would have its estimated upper radius limit of $7R_\oplus$ within the sensitivity limit of the Roman coronagraph even without

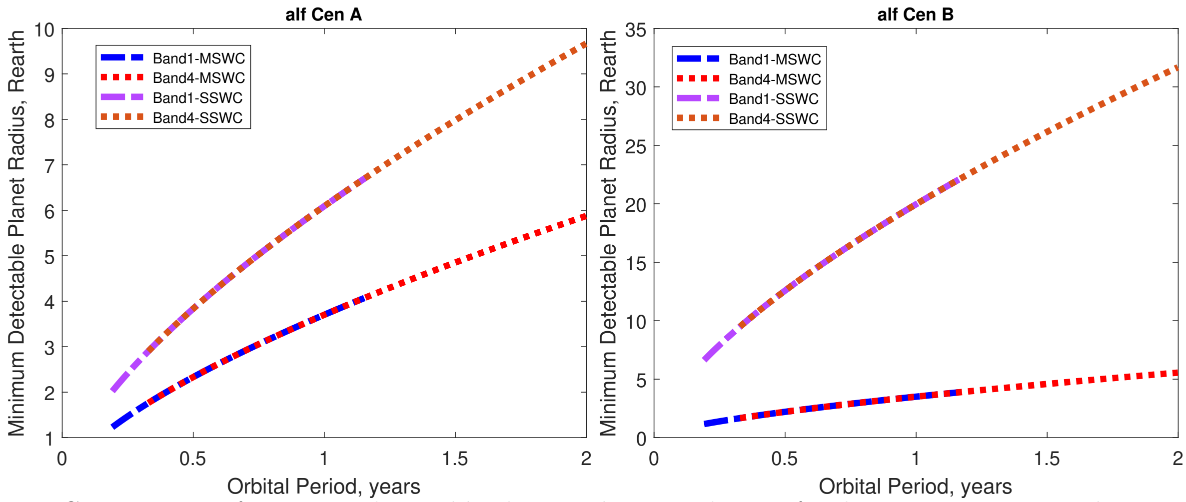

Figure 2: Computation of minimum detectable planet radii at quadrature for the Roman coronagraph instrument for both Band 1 and Band 4 assuming both contrast limited by companion leakage (SSWC) (top curves) and suppression of companion leakage (MSWC) assuming CBE levels (bottom curves) around (*Left*) Alpha Centauri A (*Right*) Alpha Centauri B.

any suppression of the companion speckles. For Alpha Centauri B, the companion's speckles would be an order of magnitude brighter, and the corresponding minimum detectable planet radius would be ∼3x larger than for Alpha Centauri A.

The bottom two curves represent the minimum detectable radii at Band 1 and Band 4 assuming suppression of the companion leakage using MSWC down to a contrast level of 1e-9. The gap between the SSWC curves at the top and the MSWC curves at the bottom shows the gain in sensitivity to minimum detectable exoplanet radii that can be achieved by suppression of companion speckles. With speckle suppression, at quadrature and near the inner working for Alpha Centauri B the minimum detectable planet radius is 1.2-1.4 $R_\oplus$ corresponding to an albedo range of 0.3-0.4 (spanning Earth-Neptune).

Previous experimental demonstrations have shown MSWC functionality reaching 1.8e-6 monochromatic contrast at the in-air testbed at NASA Ames[8,9] and with the internal source for the SCExAO instrument at Subaru.[10,11] Recently, in-vacuum demonstrations at JPL's High-Contrast Imaging Testbed (HCIT) used the Decadal Survey Testbed (DST) to demonstrate SNWC using the first diffraction order at 1.9e-9 in monochromatic light and 8.6e-9 in 10% broadband light.[12] Simulation studies have also shown compatibility with a number of different mission configurations,[13–16] including Habex/LUVOIR-B (which are arguably most similar to HWO), for the Roman coronagraph instrument, and for a planned binary star tech demo flight on PICTURE-D[17]).

In this paper, we present vacuum experimental results from the vacuum testing campaign between Nov 2021 and Jan 2022 at the Occulting Mask Coronagraph (OMC) at JPL's HCIT using the same design as the EXEP-contributed Roman MSWC mask. These represent follow-up results from last year's initial Super-Nyquist demonstrations which reached 5.1e-8 contrast in monochromatic light in a 4×4 λ/D dark zone around the 2nd diffraction order[18] (limited by the source location and range of travel available). We have installed a physical binary source on the OMC that (1) provides testing access to higher orders of the mask's diffraction grating (and in particular testing of the critical 3rd diffraction order relevant for Band 4), and (2) models the Alpha Centauri geometry to enable testing the MSWC mode. First, we reached 8.7e-9 contrast in monochromatic light in a 4×4 λ/D dark zone between 136-140 λ/D located round the 3rd diffraction order. Finally, we have demonstrated a contrast of 9.6e-8 using MSWC for the physical binary star source which is representative of an observation of Alpha Centauri A. This demonstration achieved contrast levels better than 1e-7 consistent to the required threshold technology requirement (TTR) levels. Due to the laser source available (515 nm), this required operating at a weak 5th diffraction order. An upcoming test this fall will extend the MSWC mode demonstration to the nominal 3rd diffraction order relevant to Band 3d and Band 4. A companion paper examines testbed models and limitations as well as a mitigation for estimation sensitivity to broadband light.[19]

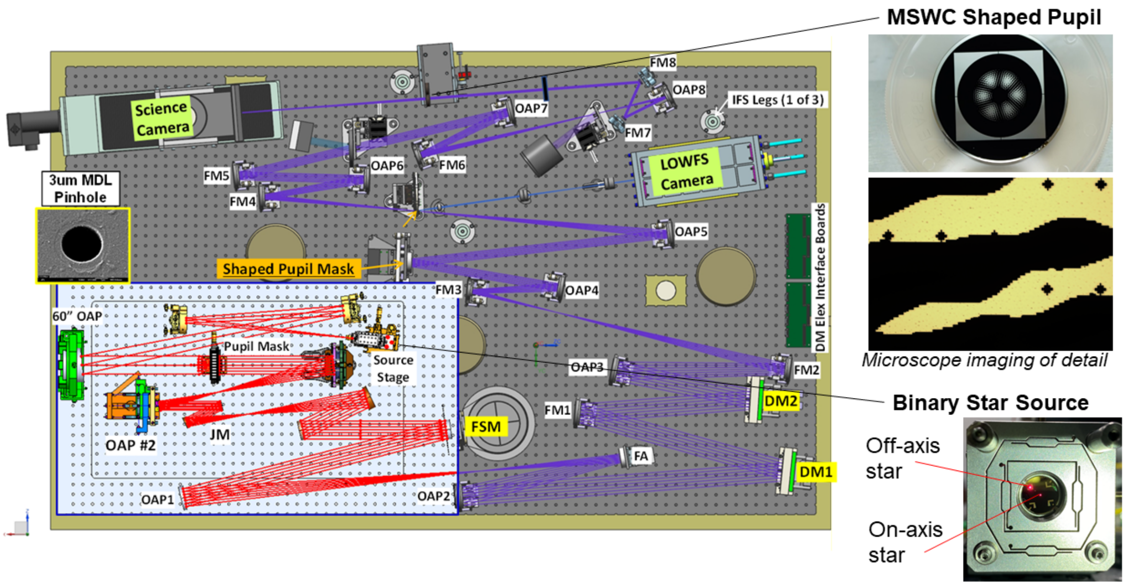

Figure 3: OMC testbed layout used for MSWC vacuum demonstration. Highlighted are the MSWC shaped pupil mask manufactured using carbon nanotubes and a microscope detail showing the array of dots forming the diffraction grating used for Super-Nyquist Wavefront control with diffraction orders evenly spaced at $\sim$47 λ/D intervals. For this vacuum test, the standard pinhole source was upgraded to a binary star source featuring an on-axis star (pinhole with 6 um diameter opening) and an off-axis star (bare fiber).

2. EXPERIMENTAL SETUP ON OMC

The current campaign is being conducted in a similar configuration to that described previously.[18] The HCIT-1 vacuum tank at JPL housing the OMC testbed is operated at 20 mTorr pressure, with the results reported here from the three-month vacuum window between November 2022 through to January 2023. The OMC was previously configured for demonstration experiments for the Roman Hybrid Lyot coronagraph (HLC) baseline mode[20,21] with minimal modifications to enable testing of the MSWC mode with the EXEP-contributed Roman MSWC shaped pupil mask design.[18] The original OMC testbed layout is shown in Figure 3, with two key modifications from the baselined HLC mode highlighted. The OMC testbed consists of a first stage simulating Roman OTA assembly including a Jitter Mirror and Fast Steering Mirror (that are generally kept in their nominal centered positions for the MSWC experiment (these do provide a small amount of source horizontal and vertical position control of up to $\sim$40λ/D). The primary change was in the addition of the MSWC shaped pupil mask. An additional modification for this testing cycle consisted is the inclusion of a new binary star source which simulates the Alpha Centauri geometry; the on-axis source is coupled to a 6 um pinhole diameter to filter aberrations (similar to the existing OMC source). The off-axis source consists of a bare-fiber separated by $\sim$4 mm distance. We use two 515 nm diode lasers that are separately fiber-fed into the vacuum chamber to simulate the mutually incoherent binary stars. The source assembly is mounted on a vertical motion stage. At this wavelength (bluer than the central wavelength of 575 nm for Band 1), the fixed-separation of the off-axis source corresponds to $\sim$240 λ/D. The wavefront control system consists of two 48x48 Northrop Grumman AOA Xinetics electrostrictive DM units with 1mm actuator spacing and separated by 1m in collimated space (with a fold mirror in-between) and similar to the flight units for the Roman coronagraphic instrument. The DMs are upstream of a Lyot-style coronagraph consisting of (1) the MSWC shaped pupil mask conjugated to the telescope pupil plane, (2) a wheel with two focal plane masks consisting of annular openings (sized for Band 1 and Band 4 similar to the available options on flight), and (3) a Lyot stop used to reject diffracted light at the focal plane. A field stop with a choice of different opening geometries controls the dynamic range between the dark zone and the bright field before final imaging onto the science camera (an Andor iXon Ultra 888).

The MSWC shaped pupil mask design for Roman is similar to the Wide-Field shaped pupil mask with the primary difference being the super-position of a square grid of dots that act as a diffraction grating[22,23] and is the same as that used in the previous vacuum test.[18] The MSWC mask is an update of the wide-field of view mask which was tested in a separate MCB testbed at HCIT.[24] The key requirement is the MSWC mask being located conjugate to the telescope pupil[25] with no vignetting of the off-axis star upstream of the location of the diffraction grating.[23] The dots cover ~3% of the total area with spacing matching the DM's actuator spacing generating a diffraction orders evenly spaced in a square grid in the focal plane at ~47 λ/D. The mask design is the same as for the EXEP-contributed mask; the mask being tested is fabricated with a carbon-nanotube process by Lambda Consulting, while the flight mask uses black silicon is manufactured by JPL's Microdevices Lab (MDL) and matches the slightly larger flight beam footprint. The mask is on a 6mm thick reflective silicon wafer substrate with silver coating, with the opaque portions covered by the growth of carbon nanotubes with 100 nm height and specular reflectivity less than 1e-7. The wafer substrate is 50.8 mm in diameter and an optical diameter of 19.6 mm. The minimum feature size on the mask is 6.7 um with each element of the diffraction grating composed of a 13-dot pattern arranged as a cross. In Figure 3, the manufactured shaped pupil mask is shown in the top-left with a microscope image detail showing the dot pattern which matches the design specification.

The focal plane mask is OD6 chrome deposited on a glass substrate with 5 mm thickness and mounted on open slots of the wheel. There are two annular openings sized for 5.6-20.4 λ/D in both Band 1 (575 nm) and Band 4 (825 nm). For these experiments, we used the Band 1 mask which was slightly larger at the 515 nm wavelength available. The Lyot stop mask is a free-standing transmissive mask manufactured by MDL with openings etched out through deep-reactive ion etching process on an gold-coated silicon wafer.

Phase retrieval[26] was used to register DMs, align the shaped pupil and Lyot stop masks, and feed initial wavefront errors to the testbed model. The resolution of the phase retrieval is given by the science camera spanning 481.2 pixels across the optical beam when imaging the pupil. An interesting observation is that registration of DM-1 shows an empirical ~0.7 actuator shift when registering using the on-axis and off-axis sources. This corresponds to a ~200 mm shift in collimated space between the pupil mask and DM-1 (which has been corrected for the upcoming vacuum test). In addition, modifications were made to the phase retrieval procedure to separately measure phase aberrations centered on a diffraction order of the off-axis star and centered on the on-axis star. This enables measurement and separate flattening of the DM corresponding to non-common path aberrations.

3. SUPER-NYQUIST WAVEFRONT CONTROL RESULTS

3.1 Experimental Sub-Nyquist Wavefront Control Baseline

We have continued usage of the FALCO open-source software package[27] to generate the testbed model and perform wavefront control using Electric Field Conjugation (EFC) wavefront control for a sub-Nyquist dark zone with pairwise probing[28] with appropriate modifications to enable both SNWC and MSWC. The testbed wavefront control uses a reduced-order implementation of the testbed layout for fast simulations. A separate testbed model is maintained for cross-comparison and with the ability to perform end-to-end modeling and limiting factor analysis and is detailed in the companion paper.[19]

We ran EFC for an 5×5 λ/D dark zone in monochromatic light with the 515 nm laser diode laser and centered along the x-axis around 13 λ/D to establish a performance baseline for single-star wavefront control which is the same size and orientation to the follow-up planned SNWC dark. We compared the ability to control the on-axis (pinhole) and off-axis (bare fiber) sources by digging single-star dark zones in the same sub-Nyquist location relative to each star. To perform a controlled experiment, we chose the same location on the science camera reachable within the travel range of the source assembly stage to center the on-axis and off-axis sources (with a small amount of horizontal motion compensated with the FSM).

Initially, the dark zone was generated without a field-stop and an enlarged area (8×8 λ/D) to reduce the bright field from 1e-5 to between 1e-6 to 1e-7 inside the dark zone and mitigate field stop edge effects. Note that these ~10 iterations constitute a separate trial and are not shown in the control history (but the ending DM state is set as the initial DM state in the two indicated runs). A field stop opening matching the dark zone was added which allowed increasing exposure times without saturation and blooming of the camera and a new

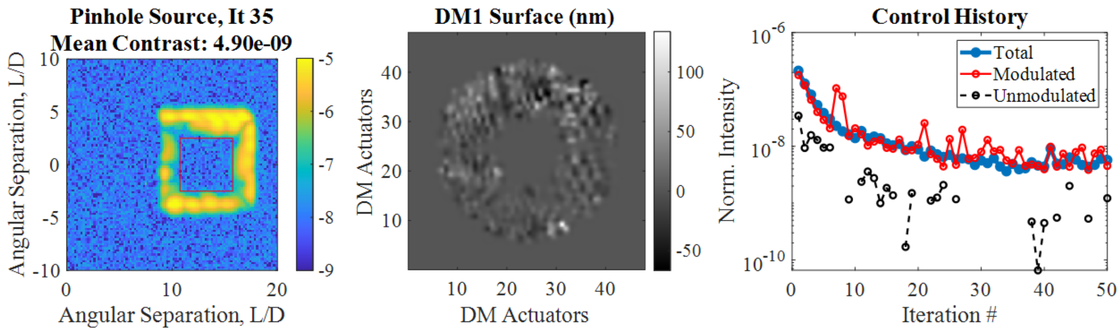

Figure 4: Baseline demonstration for sub-Nyquist single-star wavefront control with the binary star's bare fiber source placed on-axis reaches a raw contrast level of 4.9e-9 with the dominant component being modulated light. DM-1 surface used for control is estimated by the model to be 10.2 nm RMS.

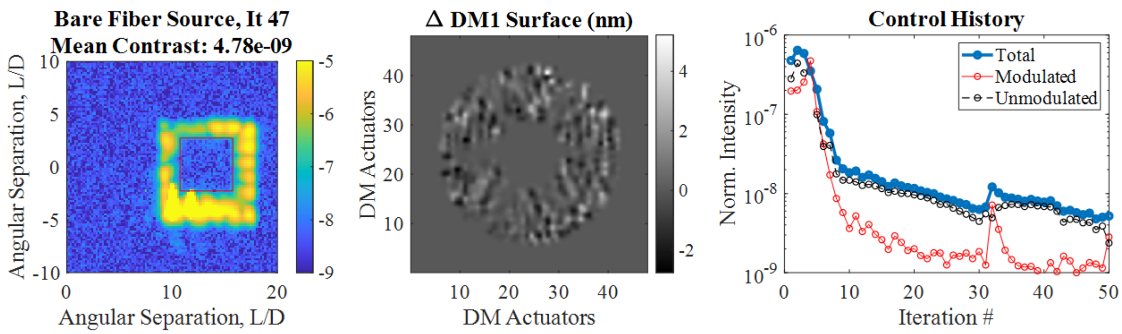

Figure 5: Baseline demonstration for sub-Nyquist single-star wavefront control with the binary star's pinhole source placed on-axis reaches a raw contrast level of 4.8e-9 with the dominant component being umodulated light. DM-1 surface is similar to the pinhole source run, with a difference of 0.5 nm RMS.

plateau limit. Two separate EFC runs were performed in a similar way corresponding to each of the binary star sources (pinhole and bare fiber) placed on-axis sequentially as described above.

The first EFC run using the pinhole source on-axis is shown in Figure 4 and reaches a contrast level of 4.9e-9 in the best iteration and using control and probing on DM-1. According to the DM model, the surface stroke used to generate this dark hole is 10.2 nm RMS.

The second EFC run uses the bare fiber on-axis and is shown in Figure 5 and reaches a very similar contrast level of 4.8e-9 in the best iteration also using control and probing on DM-1 only. The DM surface is extremely similar to that achieved for the bare fiber source, and in this case we plot the differential surface to the previous run for comparison. The difference is 0.5 nm RMS across the DM surface.

We note that these results suggest that aberrations due to the bare fiber source are similar (a potential concern which we can now rule out) and do not dominate; instead, the aberrations across the optical train are more important and placing the source in the same location yields a similar solution. We also note that coupling the source across the pinhole reduces flux level by a factor greater than 100 compared to the bare fiber. The contrast level with the binary star source is about a factor of 2x higher than with the single-star source so it is possible that there is additional incoherent scatter, but according to this baseline demonstration a contrast level of 5e-9 should, in principle, be achievable using this source.

3.2 Diffraction Order Imaging

With the addition of the binary star source and re-positioning of the source on the science camera closer to the edge (instead of centered), we now have access to higher-order diffraction orders. For the nominal pinhole on-axis source we have access to up to the 3rd diffraction order. For the bare fiber off-axis at this nominal source

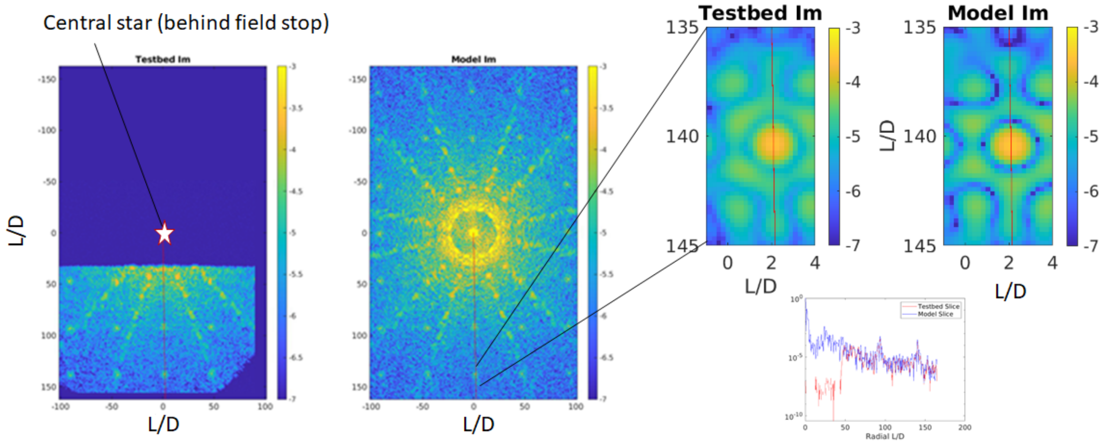

Figure 6: Comparison of testbed and model slices featuring the 3rd diffraction order created by the amplitude grating. A knife-edge field-stop is used in the testbed to prevent blooming by the stellar core. Zoom-in region is shown around the 3rd diffraction with cross-sections indicated by the solid red lines.

location (which will be used for the MSWC run), the core of the PSF falls off the camera with diffraction orders ranging from the 2nd to the 5th being visible on the camera.

A wide-field contrast-calibrated image on the camera is shown for the on-axis star compared to the expected model as shown in Figure 6 centered on the star in both cases. This represents a validation experiment to compare the diffraction order strength, morphology, and spacing with that predicted by the testbed model. The amplitude grating model is based on the shaped pupil mask specification provided for manufacture of the mask downsampled through Fourier interpolation to pupil-imaging sampling from phase-retrieval images. The central star in the testbed is blocked by the knife-edge field stop in order to prevent blooming and saturation of the camera so the diffraction orders (especially the vertical diffraction which we will use for control as these lie in the fixed direction of the off-axis, bare fiber star – which is turned off in this case) are clearly visible. We have a field of view encompassing several diffraction orders. We chose to use the 3rd diffraction order to allow SNWC testing at separations matching the Roman coronagraph Band 4 geometry for Alpha Centauri and represents an additional diffraction order distance (compared to the 2nd diffraction order in our previous vacuum test[18]). Cross-sections are indicated by the solid red lines passing through the core and through this 3rd diffraction order with a small empirically-measured rotation between the shaped pupil mask and the science camera. A zoom-in around the 3rd diffraction order is shown featuring a good match between the testbed diffraction order and the model diffraction order. First, in terms of location the diffraction order is situated at 140.4 λ/D within 0.1% (0.5 pixel) as predicted by the model. The diffraction order strength is 2.8e-4 compared to the design prediction of 3.1e-4, matching the strength within 11%. Finally, the morphology of the diffraction order is qualitatively an excellent match within a radius of 0.7 λ/D which encircles most of the core's energy, more visible differences in the speckle field can be noted outside of radius (most likely caused by non-common path errors). We do notice a slight elongation in the testbed image compared to the sharp model image which could be caused by a small amount of wavelength broadening on the laser.

The wide-field image shows 9 visible diffraction orders; automatic identification of the coordinates of visible diffraction orders from a set of pictures allows performing a least squares fit on the diffraction order grating model. An improved fit of the shaped pupil mask rotation (0.7-deg with respect to the DM), the plate scale (including a measurement of anamorphism of 0.9993), monitoring of plate scale breathing, and coordinate drifts can be empirically measured from a time-series of such wide-field images. Currently our procedure is to perform a calibration fine-tuning at the start of an EFC run to maintain a consistent match between the testbed and model across separate EFC runs. We can also perform a time-series analysis to monitor the expected level of stability. For example, in Figure 7 we show a six-hour time-series monitoring the centers of 8 diffraction

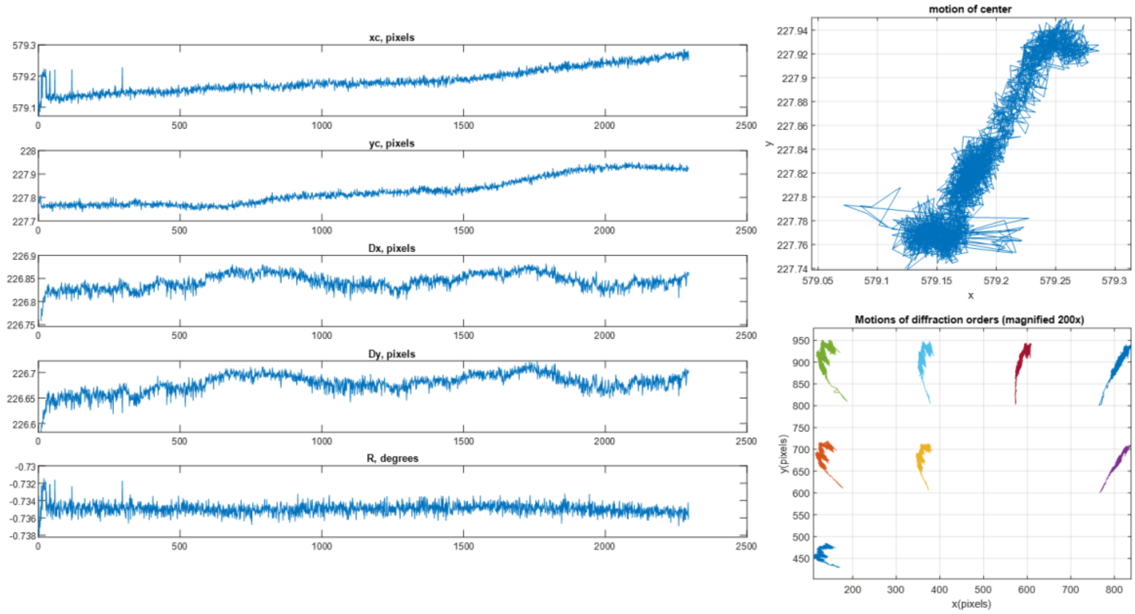

Figure 7: Time series monitoring over a 6 hour period the center of 8 diffraction orders and fitting the star center (xc and yc), geometric separation of diffraction orders (Dx and Dy from which plate scale can be estimated), and rotation angle (R). The estimated motion of the star center is shown; also shown is the motion of the individual diffraction orders magnified by a factor of 200x for visualization.

orders and compute the corresponding motion center, breathing in plate scale and rotation, and motion of the star center. The time series is consistent with the typical duration of a single EFC run at deep contrast levels and shows the stability level that can be expected during a single step. The motion of the star center can be extracted from visible diffraction orders which is relevant for determining the stellar geometry when a star falls off the camera. In addition, the motion of the diffraction orders on the camera is also shown and exaggerated to visualize stability trends. Overall, the star motion is within 0.5 camera pixel and plate scale variation is less than 0.3% which are both effects within EFC tolerance (see companion paper[19]).

3.3 Experimental Super-Nyquist Wavefront Control

Next we ran SNWC with a 5×5 λ/D correction dark zone (and using a 4×4 scoring region) located at 13 λ/D away from the diffraction order towards the stellar core (and thus between 136-141 λ/D with respect to the stellar core). This test configuration uses only the pinhole source placed on-axis. The dark zone was chosen intentionally as a similar geometry with respect to stellar core for the baseline sub-Nyquist presented previously. The FPM mask was set at an open slot as we did not need the annular open region to block the on-axis star since we were operating around the 3rd diffraction order. Note that in the next experiment with MSWC mode (and using both sources) the off-axis star's diffraction order would be within the Nyquist limit with respect to the dark zone and which would be located within the annular opening of the FPM. We used DM-1 only control and probing for this entire set of experiments.

In Figure 8 we show the best SNWC trial obtained in this test window. For this trial we used an 8×8 λ/D rectangular field stop opening from the beginning that is slightly oversized with respect to the dark zone to enable longer exposures without saturation of the camera (without the field stop, a vertical diffraction order can cause camera blooming into the dark zone); the field stop is oversized to mitigate uncorrectable field stop edge effects. The run history in the right pane excludes 30 iterations that reached a noise-limited plateau; thus starting with iteration 32 in the control history the camera exposures were increased ten-fold. The DM surface is shown in the center pane corresponding to the best iteration and we measure a SNWC correction shape with 17.3 nm RMS. The initial contrast before SNWC was 1.4e-6 and after correction this improved to 8.7e-9 representing a suppression factor of ∼160. This total intensity is composed of an estimated modulated component of 5.8e-9

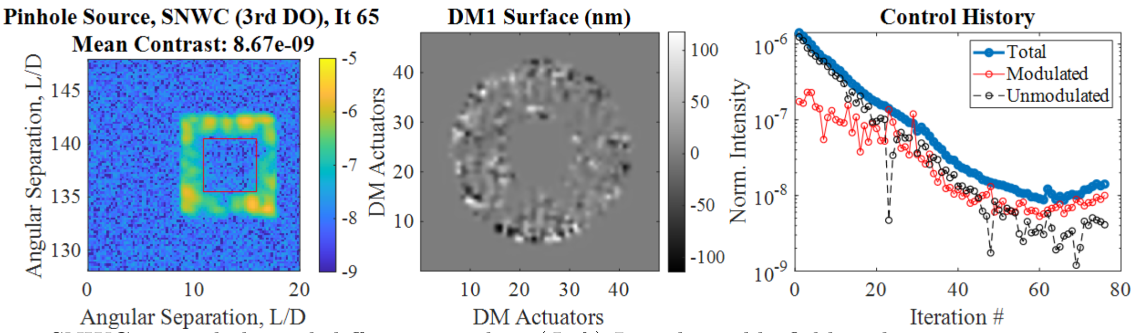

Figure 8: SNWC around the 3rd diffraction order: (*Left*) Initial speckle field with a mean starting contrast of 1.4e-6 is suppressed to a dark zone with level of 8.7e-9 (160x suppression) as indicated (*Center*) DM-1 surface after SNWC control and featuring 17.3 nm RMS (*Right*) Control history indicating the total intensity and the modulated and incoherent components which correspond at the best iteration to 5.8e-9 and 2.9e-9 respectively.

and a resulting incoherent component of 2.9e-9. This dark zone is within a factor of 1.8x of the similarly sized baseline sub-Nyquist dark zones. The cause of the contrast limited is likely model-limitations; for simulation runs when a more aggressive regularization is used deeper and faster convergence is possible to better than 1e-9.[18, 19]

A second trial achieved a slightly worse 9.6e-9 contrast levels in the same geometry and is still below 1e-8; for this second trial the total intensity was composed of a modulated component of 5.7e-9 and an incoherent component of 4.9e-9.

In terms of limiting factors, we have found that for testbed runs aggressive regularizations tend to cause divergence (including beta bumps). This affects the accuracy of probing with high initial probe correlations at the beginning of the run decreasing to low levels, which indicates possible model inaccuracies that contribute to estimation errors. A more in-depth discussion including showing model mismatch between the compact and full end-to-end models which is potentially contributing contributing to probe estimation limits is in our companion model-focused paper.[19]

4. ITERATIVE MULTI-STAR WAVEFRONT CONTROL RESULTS

With the insertion of a binary star source in the testbed, it is now possible to overcome previous mechanical limits on the current source stage assembly's travel range[18] to perform a MSWC demonstration using both the pinhole for the on-axis star and the bare fiber for the off-axis star.

The binary stars are separated by ∼4 mm which corresponds to ∼240 λ/D at the image plane for the 515 nm laser sources fed to the binary star source. For this test, we used a geometry and intensity calibration representative of observing Alpha Centauri A (on-axis) with the weaker B component off-axis. As a result, to enable MSWC it is necessary to use the nearby 5th diffraction order of the bare fiber (off-axis star). The measured strength of the peak of this diffraction order is 3.5e-5 contrast which is a factor of ∼10x weaker than the 2nd and 3rd diffraction orders used for previous SNWC tests. The SPC model also has greater error of ∼35% for this diffraction order predicting a peak with contrast of 4.7e-5. This diffraction order, moreover, shows greater deformation from low-order aberrations than the 3rd diffraction order. We used the Band 1 FPM annular opening to block the on-axis PSF core.

We utilized an iterative procedure to perform MSWC due to a testbed model limitation that required using a single DM-1 registration for each star if running these simultaneously. We found using phase retrieval that for this star separation ∼240 λ/D there is an unexpected 0.7-actuator empirical shift in the DM-1 registration. At the end of the vacuum test, this shift was identified due to piston error introduced by the shaped pupil stage with respect to the nominal reflective mirror (which served as the original reference for DM alignment).

The iterative procedure for performing MSWC was as follows. We started with a DM flat minimizing aberrations measured using phase retrieval around the 5th diffraction order. Using this initial DM flat state, we turned on the bare fiber (off-axis) source and ran SNWC EFC for 30 iterations until reaching a contrast

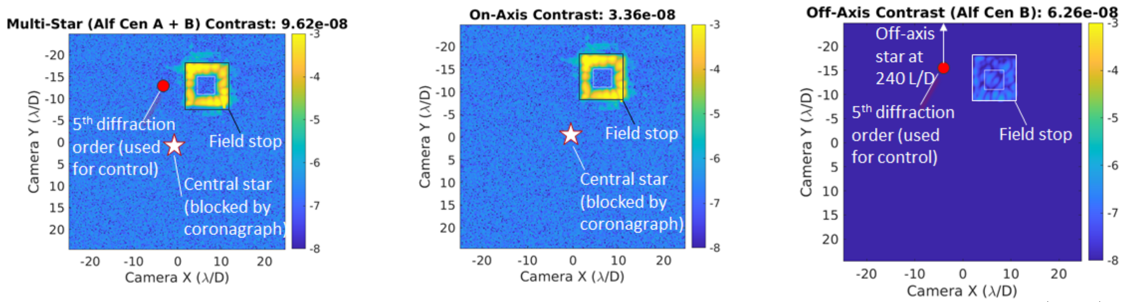

Figure 9: Multi-Star dark zone for the Alpha Centauri A + B geometry after iterative MSWC: (*Left*) Combined Alpha Centaur A and B contributions result in a dark zone with a mean contrast of 9.6e-8 (*Center*) The on-axis dark zone has a mean contrast of 3.4e-8 which is maintained after the final sub-Nyquist EFC iteration (*Right*) The off-axis dark zone has a mean contrast of 6.3e-8 contrast which has degraded from the original SNWC dark zone .

level plateau below TTR levels $\sim$ of 7.6e-8 with respect to the barefiber (i.e., Alpha Centauri B and normalized using pupil imaging since the PSF core is not directly on the camera). This corresponds to a contrast level of 2.3e-8 with respect to the pinhole (i.e., Alpha Centauri A). Maintaining this state on the DM initially, we next turned off the bare fiber and turned on the pinhole (on-axis) source and ran sub-Nyquist EFC for another 30 iterations until reaching 3.4e-8 contrast relative to Alpha Centauri A. Using this final DM state after the second iteration we measured the contrast achieved for each source independently and combined these according to an observation for Alpha Centauri A. This resulting dark zone is shown in Figure 9. Note that the contrast of the on-axis source would not significantly degrade (as shown in the figure) after the second iteration of sub-Nyquist EFC as the DM state is maintained, but the off-axis dark zone did degrade by a factor of $\sim$1.8x to 6.3e-8 due to changing the DM shape after digging the initial SNWC dark zone. We found it preferable to dig the initial dark zone with SNWC as the higher strokes required for SNWC would result in a greater degradation of the on-axis sub-Nyquist dark zone if the iterations were reversed.

5. CONCLUSIONS

We have continued demonstration of the MSWC shaped-pupil mask to enable a flight-like binary star imaging mode for the Roman coronagraph instrument. We have installed a new binary star source that simulates the Alpha Centauri stellar geometry with non-common path aberrations enabling testing of the binary MSWC mode. We have expanded the set of SNWC demonstration to the 3rd and 5th diffraction orders. In particular, we have demonstrated SNWC in a 4×4 λ/D dark zone located between 136-141 λ/D away from the stellar core and around the 3rd diffraction order at a raw contrast level of 8.7e-9 with a modulated (coherent) component of 5.8e-8 and an unmodulated (incoherent) component of 2.9e-9. We have also for the first time tested MSWC using a physical binary star source using an iterative MSWC method using SNWC around the 5th diffraction order achieving a combined multi-star dark zone for Alpha Cen A + B with a mean contrast $\sim$9.6e-8 which represents a demonstration of TTR levels. The contribution from the off-axis dark zone is 6.3e-8 and for the on-axis dark zone is 3.4e-8 so the performance is limited by the SNWC demonstrtation. In the next vacuum test window we plan to use lasers operating in Bands 3d and/or Band 4 which will potentially enable testing full MSWC with the stronger 3rd diffraction order. In addition, planned testbed model software upgrades and better alignment will also enable simultaneous MSWC at deeper contrast levels with the goal of achieving a milestone demonstration contrast level of 3e-9.

ACKNOWLEDGMENTS

This work was carried out at the High-Contrast Imaging Testbed located at the Jet Propulsion Laboratory, California Institute of Technology, and at NASA Ames Research Center. The work was supported by NASA's ISFM program. Any opinions, findings, and conclusions or recommendations expressed in this article are those of the authors and do not necessarily reflect the views of the National Aeronautics and Space Administration. J.

Hagopian at Lambda Consulting fabricated the MSWC shaped pupil mask and V. White at MDL manufactured the FPM mask. This research has made use of the Washington Double Star Catalog maintained at the U.S. Naval Observatory.

REFERENCES

[1] D. Raghavan *et al.*, "A Survey of Stellar Families: Multiplicity of Solar-Type Stars," *ApJS* **190**, 2010.

[2] A. Tokovinin, "From Binaries to Multiples. II. Hierarchical Multiplicity of F and G Dwarfs," *ApJ* **147**(4), 2014.

[3] S. Thomas, R. Belikov, and E. Bendek, "Techniques for High Contrast Imaging in Multi-Star Systems I: Super-Nyquist Wavefront Control," *ApJ* **810**(1), 2015.

[4] D. Sirbu, S. Thomas, R. Belikov, and E. Bendek, "Techniques for High Contrast Imaging in Multi-Star Systems II: Multi-Star Wavefront Control," *ApJ* **849**(2), 2017.

[5] C. Stark *et al.*, "The ExoEarth Yield Landscape for Future Direct Imaging Space Telescopes," *JATIS* **5**(2), 2019.

[6] J. Krist *et al.*, "End-to-end numerical modeling of the roman space telescope coronagraphic instrument," in *Proc. SPIE*, **12680**(12680-31), 2023.

[7] K. Wagner, A. Boehle, P. Pathak, and Y. . . V. . . I. . . O. . d. others, Journal = Nature Communications, "Imaging low-mass planets within the habitable of Alpha Centauri,"

[8] R. Belikov, E. Bendek, E. Pluzhnik, D. Sirbu, and S. J. Thomas, "High contrast imaging in multi-star systems: technology development and first lab results," in *Proc. SPIE*, **9904**, 2016.

[9] R. Belikov, E. Pluzhnik, E. Bendek, and D. Sirbu, "High-contrast imaging in multi-star systems: progress in technology development and lab results," in *Proc. SPIE*, **10400**, 2017.

[10] E. Bendek, D. Sirbu, R. Belikov, J. Lozi, O. Guyon, E. Pluzhnik, and T. Currie, "Demonstration of multi-star wavefront control using SCExAO," in *Proc. SPIE*, **11117**, 2019.

[11] E. Pluzhnik, J. Lozi, R. Belikov, D. Sirbu, E. Bendek, and O. Guyon, "Multi-star wavefront control with SCExAO instrument: demonstration with an internal source," in *Proc. SPIE*, **11823**(11823-51), International Society for Optics and Photonics, 2021.

[12] A. J. E. Riggs, G. J. Ruane, D. Sirbu, R. Belikov, and E. Bendek, "Initial super-Nyquist wavefront control experiments in the Decadal Survey Testbed," in *Proc. SPIE*, **11823**(11823-52), 2021.

[13] R. Belikov, E. Bendek, and S. Thomas, "How to directly image a habitable planet around alpha centauri with a 30-45cm space telescope,," *Proc. SPIE* **9605**, 2015.

[14] D. Sirbu, R. Belikov, E. Bendek, E. Holte, A. J. Riggs, and S. Shaklan, "Prospects for exoplanet imaging in multi-star systems with starshades," in *Proc. SPIE*, **10400**(104001D), 2017.

[15] D. Sirbu, R. Belikov, E. Bendek, C. Henze, A. E. Riggs, and S. Shaklan, "Multi-star wavefront control for the Wide-Field Infrared Survey Telescope," in *Proc. SPIE*, **10698**, 2018.

[16] D. Sirbu, R. Belikov, E. Bendek, C. Henze, and E. Pluzhnik, "Demonstration of multi-star wavefront control for WFIRST, Habex, and LUVOIR," in *Proc. SPIE*, **11117**, 2019.

[17] C. Mendillo *et al.*, "The PICTURE-C exoplanetary imaging balloon mission: laboratory coronagraph demonstrations of high-contrast imaging and low-order wavefront control," in *Proc. SPIE*, **12180**(12180-77), 2022.

[18] D. Sirbu *et al.*, "Initial laboratory demonstration of multi-star wavefront control at the occulting mask coronagraph testbed," in *Proc. SPIE*, **12180**(121802A), 2022.

[19] H. Zhou *et al.*, "Testbed multi-star wavefront control experiment modeling analysis," in *Proc. SPIE*, **12680**(12680-80), 2023.

[20] B.-J. Seo, F. Shi, B. Balasubramanian, *et al.*, "Hybrid Lyot Coronagraph for WFIRST: high-contrast broadband testbed demonstration," in *Proc. SPIE*, **10400**(10400F), 2017.

[21] B.-J. Seo, E. Cady, B. Gordon, *et al.*, "Hybrid Lyot coronagraph for WFIRST: high contrast testbed demonstration in flight-like low flux environment," in *Proc. SPIE*, **10698**(10698P), 2018.

[22] A. J. E. Riggs, D. Moody, J. Gersh-Range, D. Sirbu, R. Belikov, E. Bendek, V. P. Bailey, K. Balasubramanian, D. W. Wilson, *et al.*, "Flight mask designs of the Roman Space Telescope Coronagraph Instrument," in *Proc. SPIE*, **11823**(11823-72), 2021.

[23] E. Bendek, R. Belikov, D. Sirbu, A. J. E. Riggs, G. Ruane, and E. A. Pluzhnik, "Enabling binary stars high-contrast imaging on the Roman Space Telescope Coronagraph Instrument," in *Proc. SPIE*, **11823**(11823-54), 2021.

[24] D. Marx, E. Cady, A. J. E. Riggs, C. Prada, B. Kern, B.-J. Seo, and F. Shi, "Shaped pupil coronagraph: disk science mask experimental verification and testing," *Proc. SPIE* **10698**(10698-49), 2018.

[25] D. Marx, B. Kern, J. Krist, *et al.*, "Prediction and evaluation of the image of the WFIRST coronagraph pupil at the shaped-pupil mask," in *Proc. SPIE*, **11443**, 2020.

[26] D. Marx and B. Kern, "Phase retrieval implementation for the wfirst coronagraph development testbed," *Imaging and Applied Optics* **CT4C.4**, 2016.

[27] A. J. E. Riggs, G. J. Ruane, E. Sidick, C. T. Coker, and B. D. Kern, "Fast Linearized Coronagraph Optimizer (FALCO) I. a software toolbox for rapid coronagraphic design and wavefront correction," in *Proc. SPIE*, **10698**(106982V), 2018.

[28] A. Give'on, R. Belikov, S. Shaklan, and N. Kasdin, "Closed loop, DM diversity-based, wavefront correction algorithm for high contrast imaging systems," *Optics Express* **15**, 2007.